ELSEVIER

Contents lists available at ScienceDirect

Aerospace Science and Technology

journal homepage: www.elsevier.com/locate/aescte



Time-frequency-domain synergistic reconstruction for multi-stable deployable structure under broadband noise interference

Jiawei Qian ^{a,b}, Xiuting Sun ^{a,*}, Li Cheng ^{b,*}, Qian Lv ^a, Jian Xu ^a

ARTICLE INFO

Editor: Jae-Hung Han

Keywords:

Improved sparse reconstruction method Deployable structures Broadband noise Time-frequency-domain synergistic sindy

Time-frequency-domain synergistic sindy Optimization multi-stable structure actuation condition

ABSTRACT

Multi-stable deployable structures offer significant advantages in aerospace applications, including energyefficient configuration maintenance and switching capabilities. However, broadband noise interference from cosmic microwave background radiation, solar radiation, and spacecraft communications often compromises the accuracy of dynamic model and effectiveness of actuation strategy. To address the challenge of broadband noise interference in aerospace applications, we propose a Time-Frequency-Domain Synergistic SINDy (T-F-S SINDy) approach for accurate and robust model reconstruction, composed of four progressive criteria. First, Criterion 1 quantifies noise level through a diagnostic matrix and noise level index, determining time-domain data suitability for functions library construction and selection; Then, Criterion 2 eliminates irrelevant candidate functions via time-domain analysis when noise level meets the requirements of Criterion 1; Subsequently, Criterion 3 extracts frequency-domain features through Fourier-transformed sparse regression, followed by statistical validation using Criterion 4 to ensure model accuracy. Numerical simulations and experimental studies on multistable deployable structures demonstrate the method's effectiveness in predicting dynamic constitutive relationship expression and minimum energy deployment. The proposed framework significantly enhances robustness under broadband noise by fusing both time-domain and frequency-domain information of the systems with nonlinearity and multi-stable properties, showing broader applicability in multi-stable systems such as space deployable structures, robotic actuators, and metamaterial-based vibration isolators.

1. Introduction

Deployable structures, reconfigurable systems capable of adapting their geometric configurations to meet operational demands [1], have become indispensable in aerospace engineering (e.g., solar arrays [2,3] and satellite antennas [4,5]) and architectural engineering [6,7]. Conventional implementations predominantly employ monostable designs, including tensegrity structures [8,9], truss frameworks [10,11], and thin-walled tubular components [12,13], that require external actuation through electromechanical motors [14], pneumatic systems [15], or smart materials [16] to achieve target configurations. In recent years, multi-stable structures have attracted wide attentions from researchers owing to their rapid state transition capabilities [17], energy-efficient configuration maintaining [18], and programmable deformation pathways [19]. Introducing multi-stability in deployable structures not only eases the requirement of continuous energy supply to maintain the target configuration, but also maximizes the utilization of energy

released from configuration switching. Therefore, multi-stable property is a significant idea of inspiration for realizing deployable structures.

Accurate identification of the stable configurations of multi-stable deployable structures relies on the reconstruction of dynamic constitutive relationship. Furthermore, the Basin of Attraction (BOA), which describes the initial conditions corresponding to different states of a multi-stable system and the laws governing manifold evolution, facilitates the analysis of minimum energy deployment (MED) conditions for deployable structures by the determination of critical initial conditions for dynamic state switching in multi-stable systems through its boundaries. Both of the aforementioned tasks need to be achieved by accurate dynamic modeling. Thus, methods for establishing accurate dynamic models of multi-stable deployable structures are of great importance. Traditional approaches employing first-principles methods, including Newton-Raphson scheme [20] and Lagrangian equations [21], remain prevalent for deriving system governing equations. These theoretical methods offer dual advantages: reduced computational complexity and enhanced model interpretability. However, their practical applications

E-mail addresses: 05mech_sunxiuting@tongji.edu.cn (X. Sun), li.cheng@polyu.edu.hk (L. Cheng).

a School of Aerospace Engineering and Applied Mechanics, Tongji University, Shanghai, China

b Department of Mechanical Engineering, The Hong Kong Polytechnic University, Kowloon, Hong Kong, China

^{*} Corresponding authors.

Nomenclature

SINDy Sparse Identification of Nonlinear Dynamics T-F-S SINDy Time-Frequency-domain Synergistic sparse

identification of nonlinear dynamics

SNR Signal-to-Noise Ratio BOA Basin of Attraction

PCA Principal Component Analysis

PC Principal Component NLI Noise Level Index DOF Degree-of-Freedom

MED Minimum Energy Deployment LSTM Long Short-Term Memory GRU Gated Recurrent Unit RNN Recurrent Neural Network

often necessitate simplifying assumptions that may compromise model accuracy. Furthermore, even with the correct model form, parameter identification remains essential for system characterization and behavior prediction. In contrast to first-principles modeling, data-driven approaches enable direct reconstruction of governing equations from data of input and output variables. Recent advances in machine learning have yielded numerous techniques for physical law discovery from experimental data. Among these, neural network-based implicit methods establish input-output mappings through nonlinear activation functions and optimized weight [22,23]. Enhanced variants like LSTM [24,25] and GRU [26] networks further mitigate gradient-related challenges inherent in RNNs. Despite their flexibility, these black-box models inherently lack explicit governing equations, resulting in limited interpretability and generalization capability.

Explicit regression-based methods provide an alternative paradigm to construct analytical relationships between variables. The most widely used regression method is Least squares regression [27], where the coefficients are obtained by minimization of mean squared error. Furthermore, sparse regression methods, such as Lasso regression [28] and ridge regression [29], are proposed to avoid overfitting by introducing regularization [30]. The Sparse Identification of Nonlinear Dynamics (SINDy), introduced by Brunton et al. [31], exemplifies this approach through its integration of sparse regression and machine learning to reconstruct ordinary differential equation-based system models. Subsequent extensions have adapted SINDy for partial differential equations [32], variational formulations [33], delay differential systems [34] and stochastic dynamical equations [35], expanding its applications across physics [36], fluid dynamics [37], and robotics [38, 39]. However, the application of such data-driven methods to spaceborne deployable structures presents unique challenges. The operational environment introduces broadband interference from cosmic microwave background radiation, solar emissions, and inter-satellite communications. Such high-noise conditions particularly compromise SINDy's performance due to its sensitivity to measurement uncertainties. This limitation highlights a critical research gap in feature extraction and enhancement during regression-based equation discovery, particularly for systems operating under significant stochastic disturbances.

This paper addresses the challenges of broadband strong noise interference in deployable structure reconstruction by proposing a Time-Frequency-Domain Synergistic SINDy (T-F-S SINDy) method that synergistically utilizes time-domain and frequency-domain response characteristics. The methodological innovation lies in the strategic integration of time-domain and frequency-domain features to enhance reconstruction robustness. The proposed framework establishes four fundamental criteria: Criterion 1 evaluates time-domain data suitability for library selection, Criterion 2 governs library function determination,

Criterion 3 implements spectral band truncation to preserve high Signal-to-Noise Ratio (SNR) components, and Criterion 4 establishes statistical validation metrics for model accuracy. Numerical simulations and experimental validation demonstrate the efficacy and applications of this data-driven approach. The paper organization follows a systematic progression: Section 2 formalizes the problem statement and details the reconstruction methodology; Section 3 presents numerical verification through two case studies; Section 4 applies the method to derive governing equations for a multi-stable deployable structure unit cell in the experiments, and Section 5 concludes with key findings and implications.

2. Sparse reconstruction of dynamic model for deployable structures

2.1. Dynamic model for deployable structures with multi-stable property

Various frame structures are used in satellites as deployable space antenna, which requires sufficient but saving-energy actuation for switching the deployed configuration, as shown in Fig. 1(a). For the deployable structures, both nonlinear force-displacement relationship with variable-stiffness property and actuation condition for deployed configuration can be determined based on accurate dynamic model. As illustrated in Fig. 1(b), quasi-static tension/compression tests are commonly adopted to obtain the force-displacement relationship in the conventional ground tests, which is particularly effective for structures with monostable property. Unfortunately, conducting quasi-static tests on the deployable structures with multi-stable property to predict dynamic behaviors would involve significant limitations. The forcedisplacement relationship derived from the quasi-static tests and analysis diverge from those observed in dynamic processes; And critical dynamic factors including equivalent dissipation effects cannot be adequately captured. These limitations fundamentally stem from the inherent absence of dynamic system information in quasi-static methodologies, necessitating the development of dynamic model reconstruction techniques, as shown in Fig. 1(c). Dynamic approaches can reconstruct accurate analytical dynamic model from regression of inputs and responses, enabling both force-displacement relationship prediction in dynamic processes and MED analysis via BOA.

The regression process from dynamic information is briefly introduced as follows. Without loss of generality, the analytical dynamic model for multi-stable deployable structures can generally be expressed by the following governing equation

$$\dot{\mathbf{x}}(t) = \mathbf{F}(\mathbf{x}(t), \mathbf{u}(t)),\tag{1}$$

where $\mathbf{x}(t)$ and $\dot{\mathbf{x}}(t)$ represent the state variables and their derivatives, respectively, and $\mathbf{u}(t)$ denotes the time-varying input of the system. Considering that in different environments, both functional form and term coefficient of $\mathbf{F}(\bullet)$ could be different, the regression process aims to identify both the functional form and parameters through dynamic responses of system under the dynamic input $\mathbf{u}(t)$. To transform the model reconstruction problem into a sparse regression problem, it is assumed that the derivative terms can be expressed as a linear combination of candidate functions. Then, by constructing a comprehensive library of candidate functions encompassing state variables and system inputs, the regression problem can be formulated as

$$\dot{\mathbf{x}}(t) = \mathbf{\Theta}(\mathbf{x}(t), \mathbf{u}(t))\mathbf{\Xi},\tag{2}$$

where $\Theta(\mathbf{x}(t), \mathbf{u}(t)) \in \mathbb{R}^{m \times n}$ is the function library constructed by candidate functions of state variables and system inputs, and Ξ denotes the coefficients corresponding to candidate functions. The fundamental challenge lies in minimizing the residual between actual and reconstructed derivative terms, leading to various optimization formulations. The most commonly used regression method is the Least squares regression [27], whose objective function writes

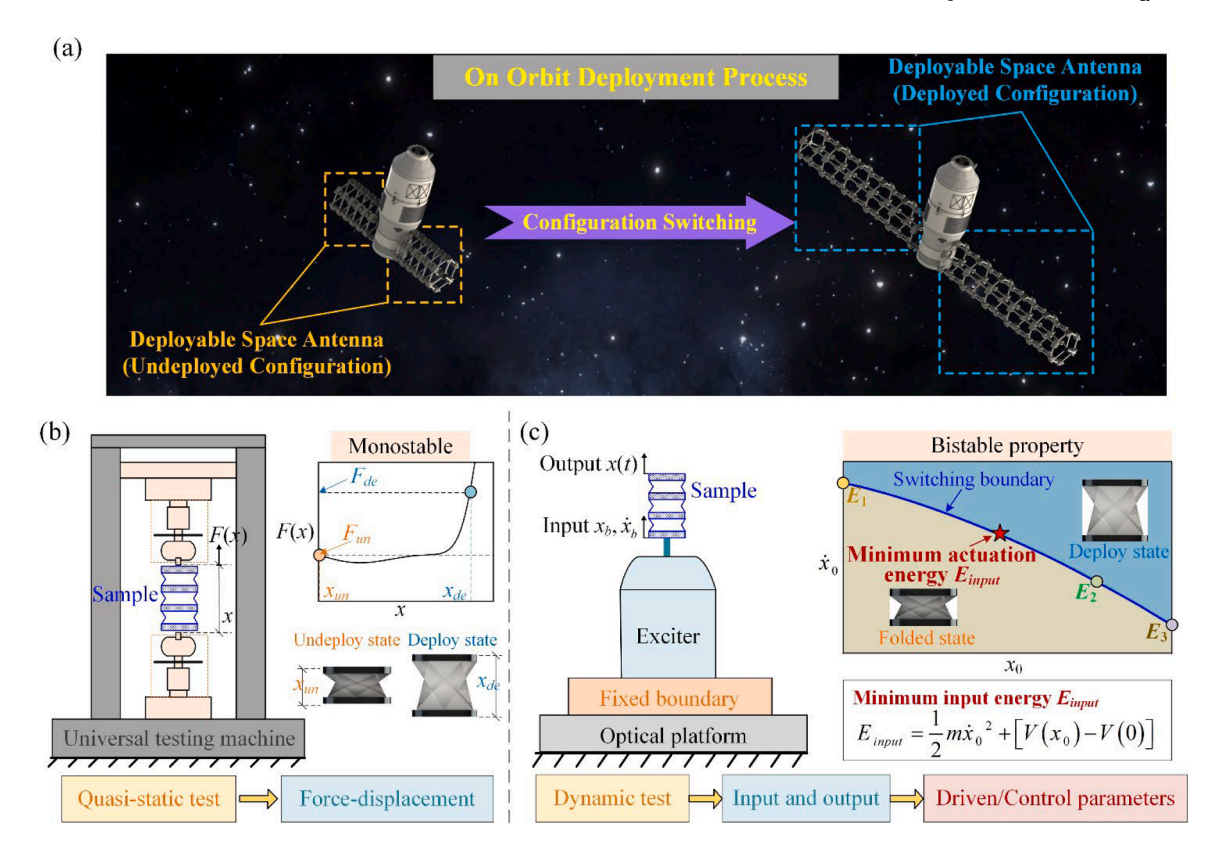


Fig. 1. Different approaches to analyze the force-displacement relationship and MED conditions of the deployable structures with multi-stability property. (a) The application of deployable structures in aerospace, which needs dynamic modeling reconstruction for energy-saving actuation condition for deploying; (b) Quasi-static approach and the static force-displacement relationship. (c) Dynamic approach for dynamic model reconstruction and the BOA based actuation energy definition.

$$\mathbf{\Xi} = \operatorname{argmin} \| \mathbf{\Theta} \mathbf{\Xi} - \dot{\mathbf{x}} \|_{2}. \tag{3}$$

Considering that the dynamic behaviors of physical systems are usually dominated by a few terms in the governing equations, SINDy (proposed in Ref. [31]) is adopted with the following objective function with L_1 regularization to consider the sparsity of the model so that the interpretability and generalization ability could be improved, written as

$$\boldsymbol{\mathcal{Z}} = \operatorname{argmin}(\|\boldsymbol{\Theta}\boldsymbol{\Xi} - \dot{\boldsymbol{x}}\|_{2} + \lambda \|\boldsymbol{\mathcal{Z}}\|_{1}). \tag{4}$$

By introducing L_1 -penalty term, objective function Eq. (4) imposes constraints on the number of terms in the reconstruction model, thus improving the sparsity of the model. Practical implementation in aerospace applications faces significant challenges from broadband noise contamination in measured state variables. Cosmic microwave background radiation, solar/terrestrial radiation, and inter-satellite communication signals introduce spectral interference that particularly affects time-domain regression methods. Furthermore, elevated noise levels can interrupt with the characteristics of the multi-stable system and ultimately lead to algorithm failure. To address these challenges, this study proposes a T-F-S SINDy method for reconstructing robust governing equation of the multi-stable deployable structures operating under broadband noise conditions.

2.2. Improved T-F-S SINDy methodology

This section elaborates the improved model reconstruction methodology by the definition of four criterion, with the algorithmic workflow systematically presented in Fig. 2. The process initiates with narrow-band excitation to generate system responses for function library construction. A noise level metric is subsequently established to quantify the SNR of acquired time-domain data, enabling application of **Criterion 1** for assessing data quality suitability in library selection. If the SNR of the collected data satisfies Criterion 1, the time-domain data

is utilized to eliminate the most irrelevant candidate functions according to **Criterion 2**. The proposed improved methodology then transitions to frequency-domain analysis, and **Criterion 3** facilitates noise-resilient capability via frequency characteristic extraction. The refined data is integrated by data assembly principle, and the subsequent sparse regression method is used to solve the inverse problem. Ultimately, **Criterion 4** provides validation of model accuracy through statistical metrics of residual error. By the proposed improved model-reconstruction method, called T-F-S SINDy method, concise and accurate dynamic model can be obtained with significant applicability.

2.2.1. Criterion 1: Noise level estimation

For broadband noise environment such in aerospace, the governing equations of multi-stable systems are reformulated as

$$\dot{\mathbf{x}}(t) = \sum_{i=1}^{k} \xi_i \mathbf{f}_i(\mathbf{x}(t) + \mathbf{e}(t), \mathbf{u}(t) + \mathbf{e}(t)), \tag{5}$$

where $\mathbf{e}(t)$ represents the broadband measurement/environment noise. Given the inherent sparsity of governing equations, the condition k < n holds. Eq. (5) reveals that when $\mathbf{e}(t)$ remains sufficiently small, system derivatives can be approximated through sparse linear combinations of candidate functions. Conversely, elevated noise levels violate the fundamental governing equations Eq. (2), rendering such sparse representations invalid. This enables noise quantification through collinearity analysis between derivative signals and candidate functions. Noise estimation framework is developed through the following procedure: First, the diagnostic matrix \mathbf{B} is constructed as

$$\mathbf{B} = [\mathbf{\Theta}(\mathbf{x}(t), \mathbf{u}(t))\dot{\mathbf{x}}(t)],\tag{6}$$

which contains candidate functions and derivative terms. Then, Principal Component Analysis (PCA) is applied by conducting singular value

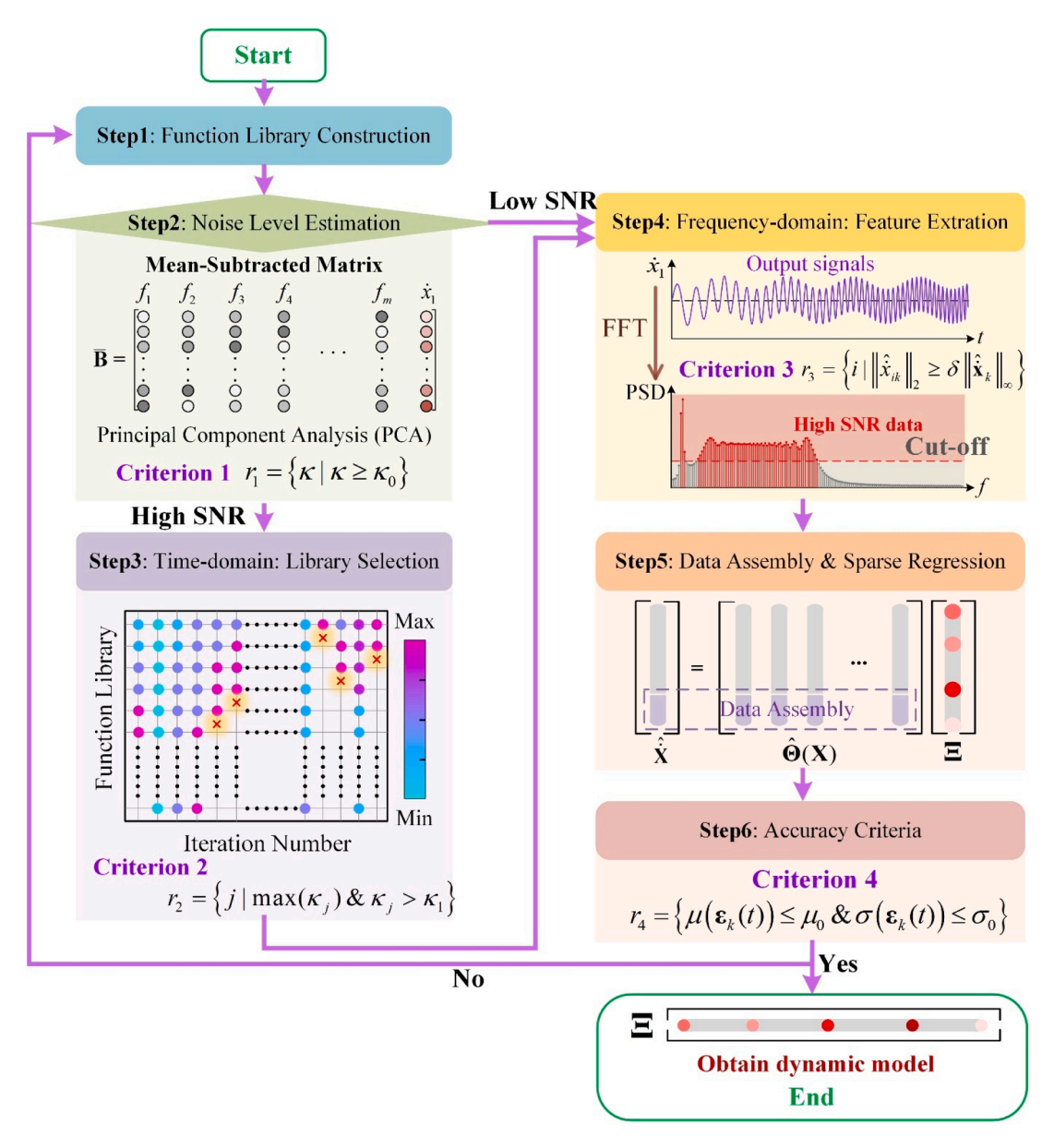


Fig. 2. Algorithm flow chart of the proposed time-frequency-domain synergistic reconstruction method with four criteria.

decomposition to mean-centered $\overline{\mathbf{B}}$, as

$$\overline{\mathbf{B}} = \mathbf{B} - \frac{1}{m} \mathbf{J} \mathbf{B} = \mathbf{U}_B \mathbf{\Sigma}_B \mathbf{V}_B, \tag{7}$$

where $\mathbf{J} \in \mathbb{R}^{m \times m}$ represents all-ones matrix. The columns of \mathbf{V}_B are the Principal Components (PCs) of matrix \mathbf{B} , and diagonal elements of Σ_B (σ_i) are the square root of eigenvalues corresponding to each PC (λ_i). The minimum eigenvalue λ_{m+1} vanishes under noise-free conditions ($\mathbf{e}(t)$) \equiv 0). The Noise Level Index (NLI) is subsequently defined as

$$\kappa = \log_{10} \frac{\lambda_1}{\lambda_{m+1}}.\tag{8}$$

This index is equivalent to the condition number of covariance matrix of ${\bf B}$, serving as a quantitative measure of column-wise collinearity degradation caused by noise. Higher NLI values indicate better SNR. Based on NLI, the first Criterion r_1 is proposed as

$$r_1 = \{\kappa | \kappa \ge \kappa_0\},\tag{9}$$

where a threshold κ_0 is established to distinguish high-SNR (NLI $\geq \kappa_0$)

from low-SNR (NLI< κ_0) regimes, enabling automated data quality assessment.

2.2.2. Criterion 2: Library selection from time-domain information

When state variables and system inputs exhibit high SNR measurements, the rich information of time-domain data can be exploited to pre-filter candidate functions in the functions library, thereby significantly reducing the regression dataset requirements. Building upon the proposed NLI, we establish the second criterion in the improved T-F-S SINDy methodology for library selection, formulated as

$$r_2 = \{j | \max(\kappa_j) \& \kappa_j > \kappa_1\}, \tag{10}$$

where j is the index of the eliminated candidate function; κ_j the resultant NLI after removal j^{th} candidate function and κ_1 the NLI threshold. The basic idea of the criterion r_2 stems from the observation that removing non-essential candidate functions that are unrelated to derivative representation maintains the function library's ability to express derivatives through linear combinations of remaining candidate functions, thereby preserving NLI values above critical thresholds. Through iterative

elimination of candidate functions demonstrating minimal reduction in NLI while sustaining high NLI values, the proposed methodology can effectively prune extraneous candidate functions from the library.

2.2.3. Criterion 3: Feature extraction from frequency-domain analysis

From time-domain analysis, noise contamination permeates every discrete time-step in the measurement, with individual time-domain noise intensity being inherently challenging to quantify. Conversely, frequency-domain analysis reveals distinct spectral characteristics: under narrow-band excitation, system responses concentrate in specific frequency bands while noise distributes uniformly across the wide spectrum. This frequency segregation enables system response features to dominate over noise in their characteristic bands, manifesting as enhanced amplitude and superior SNR. Capitalizing on this spectral disparity, frequency-domain sparse regression effectively isolates noise from essential system features, thereby enhancing algorithmic robustness and identification accuracy under low-SNR conditions. The methodology initiates with Fourier transformation of the governing equations, yielding the frequency-domain regression formulation

$$\widehat{\dot{\mathbf{x}}} = \mathbf{V}\dot{\mathbf{x}}(t) = \mathbf{V}\Theta(\mathbf{x}(t), \mathbf{u}(t)) \mathbf{\Xi} = \widehat{\boldsymbol{\Theta}}\mathbf{\Xi}, \tag{11}$$

where V is the Fourier transformation matrix; $\hat{\mathbf{x}}$ and $\hat{\Theta}$ the derivative terms and function library in frequency-domain. Recognizing that high-amplitude frequency components inherently correspond to high-SNR regions, we propose selection criterion r_3 as

$$r_3 = \{i \mid \mid \widehat{\mathbf{x}}_{ik} \mid \mid_2 \ge \delta \mid \mid \widehat{\mathbf{x}}_k \mid \mid_{\infty} \}. \tag{12}$$

This criterion retains frequency components where response amplitudes exceed $\delta \| \hat{\mathbf{x}}_k \|_{\infty}$, with $\| \hat{\mathbf{x}}_k \|_{\infty}$ denoting the maximum amplitude in the k^{th} derivative spectrum domain (k^{th} column of derivative matrix $\hat{\mathbf{x}}$), $\| \hat{\mathbf{x}}_{ik} \|_2$ representing the i^{th} frequency amplitude in the k^{th} derivative spectrum, and δ defining the cut-off threshold ratio. Through this spectral feature extraction, the sparse regression problem is rigorously formulated as

$$\widehat{\dot{\mathbf{x}}}_{r}(i,k) = \widehat{\Theta}(i,j) \ \Xi(j,k), i \in r_{3}, j \in r_{2}, k = 1, ..., n_{y}, \tag{13}$$

where n_y denotes the number of the Degree-of-Freedom (DOF) for succinctly describing the dynamic responses of the system.

2.2.4. Criterion 4: Accuracy and algorithm iteration

Following the time-frequency-domain synergistic procedure, the refined derivative matrix and function library matrix are systematically integrated through the data assembly principle established in our prior work [39]. The coefficients in the governing equation are subsequently obtained by applying sparse regression to Eq. (13). To quantitatively guarantee the accuracy of the reconstruction dynamic model, we formulate the fourth criterion r_4 that simultaneously evaluates model precision and reliability. The discrepancy between the true system response $\dot{\mathbf{x}}(t)$ and reconstructed response $\tilde{\dot{\mathbf{x}}}(t)$ is modeled as a random variable, as

$$\boldsymbol{\varepsilon}(t) = \dot{\mathbf{x}}(t) - \widetilde{\dot{\mathbf{x}}}(t),$$
 (14)

whose statistical properties reflect two distinct error sources: systematic model inaccuracies and stochastic measurement noises. The error components exhibit fundamentally different characteristics: modelinduced deviations demonstrate stability and pattern consistency, whereas errors caused by purely measurement noise contributes unbiased random fluctuations. For accurate reconstruction model, the expectation μ of the random variable ϵ should be very close to zero. Concurrently, the variance σ of ϵ serves as an indicator of model reliability, with lower variance values corresponding to higher confidence in the reconstruction model. This dual-aspect evaluation leads to the

following accuracy criterion, given as

$$r_4 = \{ \mu(\varepsilon_k(t)) \le \mu_0 \& \sigma(\varepsilon_k(t)) \le \sigma_0 \}, \tag{15}$$

where μ and σ are the expectation and variance of the difference variable $\epsilon.$

2.2.5. Overall procedure of T-F-S SINDy

By integrating the proposed four criteria, the overall workflow of the proposed T-F-S SINDy method is shown in Fig. 2, whose reconstruction procedure can be summarized as follows:

Step 1: Collect the dynamic response data of multi-stable deployable structure under narrow-band sweep excitation at a specific configuration and construct the corresponding function library matrix.

Step 2: Calculate the diagnostic matrix **B** using Eq. (6), and further apply Eq. (7) to perform principal component analysis on the diagnostic matrix **B**. After computing NBI by Eq. (8), the noise level of the response data is determined by Criterion 1.

Step 3: If the noise level belongs to low SNR category, proceed to the next step; otherwise, employ Criterion 2 to pre-filter candidate functions library functions based on the time-domain information of the response.

Step 4: Transfer the regression problem into the frequency domain by Fourier transform, and implement spectral band truncation to preserve high SNR components by Criterion 3.

Step 5: Apply the data assembly principle [39] to assemble the refined function library matrix corresponding to different configurations, and conduct the sparse regression method [31] to obtain the reconstruction model.

Step 6: Criterion 4 is adopted to evaluate the accuracy. If Criterion 4 is satisfied, the reconstruction model can be obtained; otherwise, repeat the process until Criterion 4 is satisfied.

3. Numerical verifications

3.1. A deployable unit cell structure with bi-stable property

The reconstruction methodology is first validated through a bi-stable deployable unit cell under varying broadband noise conditions. The schematic diagram of the bi-stable deployable unit cell is shown in Fig. 3 (a), which is so-called Kresling Origami structure. The dynamic modeling process of the Kresling origami structure is illustrated in Appendix A. As Refs. [40,41], with structural parameters a=1.6, c=1, $\gamma_0=30^\circ$, the potential energy for different axial deformation is shown in Fig. 3(b), demonstrating bi-stable property. On the potential energy curve, two local minimum points correspond to undeployed state (S1) and deployed state (S2). For the unit cell, vibration inputs with white Gaussian noise for high-SNR (60 dB) and low-SNR (30 dB) are given. A seventh-order polynomial function library is employed for model reconstruction. The reconstruction process is systematically evaluated through four proposed criteria as Figs. 3(d)-(f).

The first criterion r_1 in T-F-S SINDy method quantifies measurement noise levels through zero-mean Gaussian noise analysis (Fig. 3(c)). The metric effectively discriminates signal quality thresholds, particularly demonstrating heightened sensitivity below 30 dB where time-domain data becomes unreliable. As shown in Fig. 3(c) that NBI remains at a high level and does not show a significant downward trend when SNR is slightly reduced at high SNR levels. Conversely, at low SNR levels, not only is NBI small, but it also exhibits a clear downward trend as SNR decreases. Therefore, for Criterion 1, the threshold of NBI can be determined by continuously increasing noise until NBI shows a significant decrease. Subsequent application of criterion r₂ under SNR=60 dB (Fig. 3(d)) successfully prunes non-essential terms while preserving governing equation components through NLI ranking. The threshold for Criterion 2 is determined by monitoring the variation of NBI throughout the candidate function elimination process and selecting the NBI value before the phase of abrupt decrease. From frequency-domain analysis,

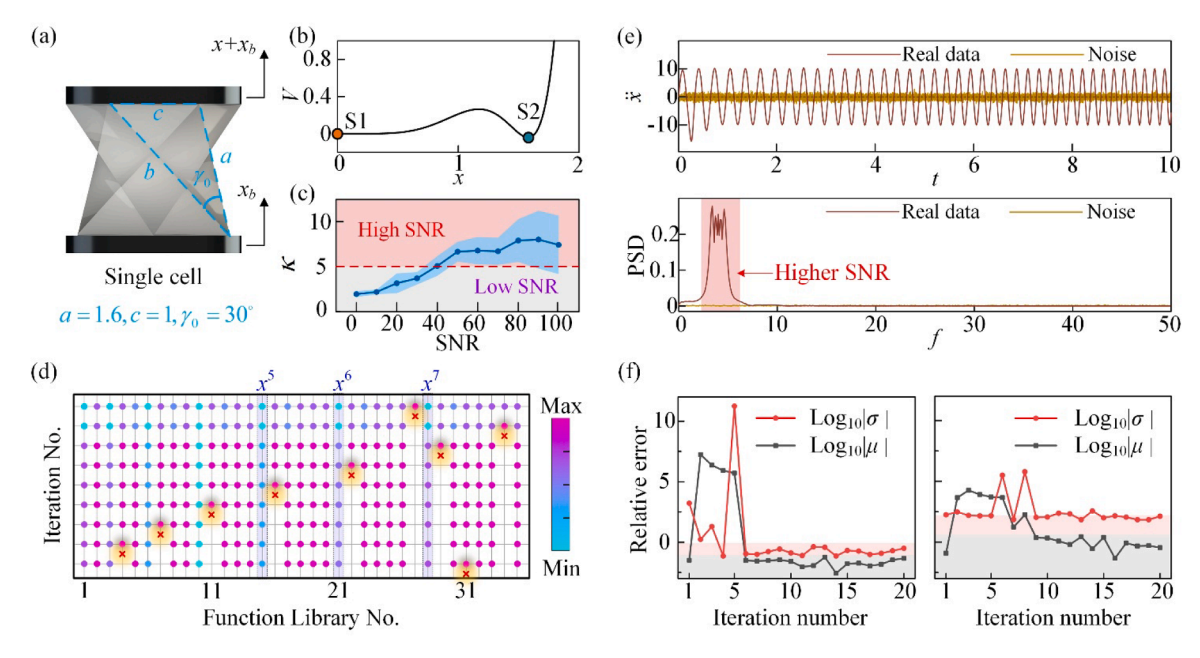


Fig. 3. Schematic diagram of the bi-stable deployable unit cell and the reconstruction process. (a, b) Mechanical schematic diagram and the potential energy of the bi-stable deployable unit cell. (c) Noise level estimation criterion r_1 under different noise level. Schematic diagram of (d) time-domain library selection process, (e) frequency-domain feature extraction and (f) accuracy criterion.

criterion r_3 (Fig. 3(e)) enhances the quality of the data by exploiting spectral separation: system responses concentrate in narrow bands while noise distributes broadly, enabling effective frequency-domain feature extraction. Final model validation via accuracy criterion r_4 (Fig. 3(f)) shows rapid convergence of expectation (μ) and variance (σ). The changing trends of the mean and variance for difference variable ε during the iterative data assembly process are observed, with the thresholds determined by excluding initial-stage reconstruction models exhibiting high mean or variance while retaining those converging to low mean and low variance. Besides, it could also be observed that by combining time-domain information, the converge process is accelerated since the number of candidate functions is greatly reduced.

By the proposed model reconstruction method as above, the reconstruction model of the unit cell is

$$\ddot{x} + \zeta \dot{x} + \alpha x^5 + \beta x^6 + \gamma x^7 = 0, \tag{16}$$

where the corresponding coefficients for SNR=60 dB and 30 dB are shown in Table 1. Reconstruction models demonstrate faithful reproduction of essential system characteristics in Fig. 4.

Fig. 4(a, b) shows excellent agreement between actual and reconstructed potential energy and restoring force profiles across both SNR conditions. BOA predictions (Fig. 4(c-f)) achieve 0.94 % (60 dB) and 2.46 % (30 dB) error rates, confirming the robustness of the method. These BOA solutions enable MED analysis. The actuation input for deployment is equivalent to the initial conditions of the bi-stable deployable unit cell $x(0) = x_0$, $\dot{x}(0) = \dot{x}_0$. In order to quantify the input energy, the input energy for deployment is defined as

$$E_{\rm in} = \frac{1}{2} m \dot{x}_0^2 + (V(x_0) - V(x_{\rm S1})), \tag{17}$$

Table 1Reconstruction model coefficients for different SNR in deployable unit cell structure with bi-stable property case.

SNR	ζ	α	β	γ
60dB	1.99	12.12	-18.03	6.56
30dB	1.98	10.66	-16.05	5.88

which combines kinetic energy and potential energy increments. Phase-plane analysis (Fig. 4(g-h)) reveals consistent MED conditions at switching boundaries, demonstrating that MED can be realized through initial displacement inputs. This is a physical consequence of the reduced damping dissipation in displacement inputs. The proposed T-F-S SINDy is compared with the classical SINDy in terms of both computational efficiency and reconstruction accuracy, and the results are demonstrated in Appendix B.

Method validation extends to pink noise environments as shown in Fig. 5, maintaining comparable accuracy in potential energy reconstruction, BOA prediction, and MED analysis. Particularly noteworthy is the method's resilience to 1/f noise spectral characteristics, where traditional frequency-domain techniques typically degrade due to the enhanced low-frequency interference.

3.2. A M-DOF deployable structure with multi-stable property

In this case, the model reconstruction of a M-DOF deployable structure with multi-stable property is demonstrated. Fig. 6 presents the deployable structure, comprising serially connected Kresling Origami cells. Fixing structural parameters in Cell 1 as a_1 =1.6, c_1 =1, γ_1 =20° and Cell 2 as a_2 =1.6, c_2 =1, γ_2 =28.5°, two cells respectively exhibit monostable and bi-stable properties. The dual objectives of model reconstruction are detecting monostable configurations from design imperfections and determining MED condition through BOA analysis. In order to accomplish these two objectives, not only the number and the location of each layer need to be correctly identified, but also the damping terms need to be accurately reconstructed to achieve a good prediction of BOA. Compared with the S-DOF case, the number of candidate functions in the function library dramatically increases due to the increasing number of state variables in the M-DOF case, making it more difficult to reconstruct the accurate model of the system.

Following the proposed T-F-S SINDy method with four criteria, two reconstruction processes are performed under white noise environments at 60 dB and 30 dB SNR, respectively. By the proposed T-F-S SINDy method with the signals shown in Fig. 6(c), the reconstruction model of the M-DOF deployable structure with multi-stable property is obtained

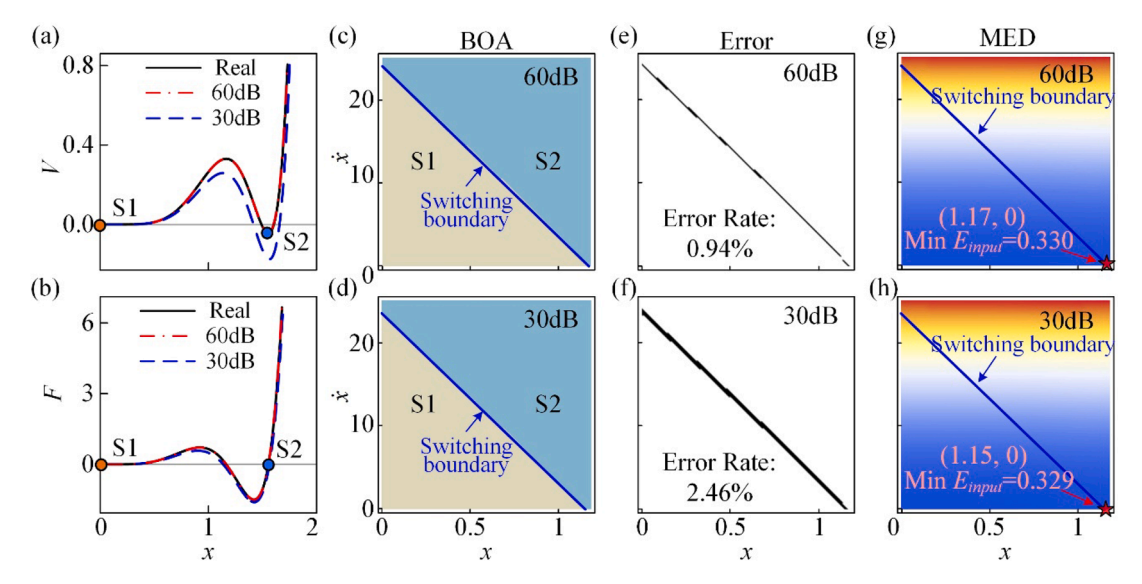


Fig. 4. Model reconstruction results for the bi-stable deployable unit cell under white Gaussian noise. (a) Comparison of potential energies among the real model, reconstructed models with different noise levels. (b) Comparison of restoring forces among the real model, reconstructed models with different noise levels. (c-f) BOA prediction and corresponding error comparison under different noise levels. (g)-(h) show the MED prediction from the reconstructed models.

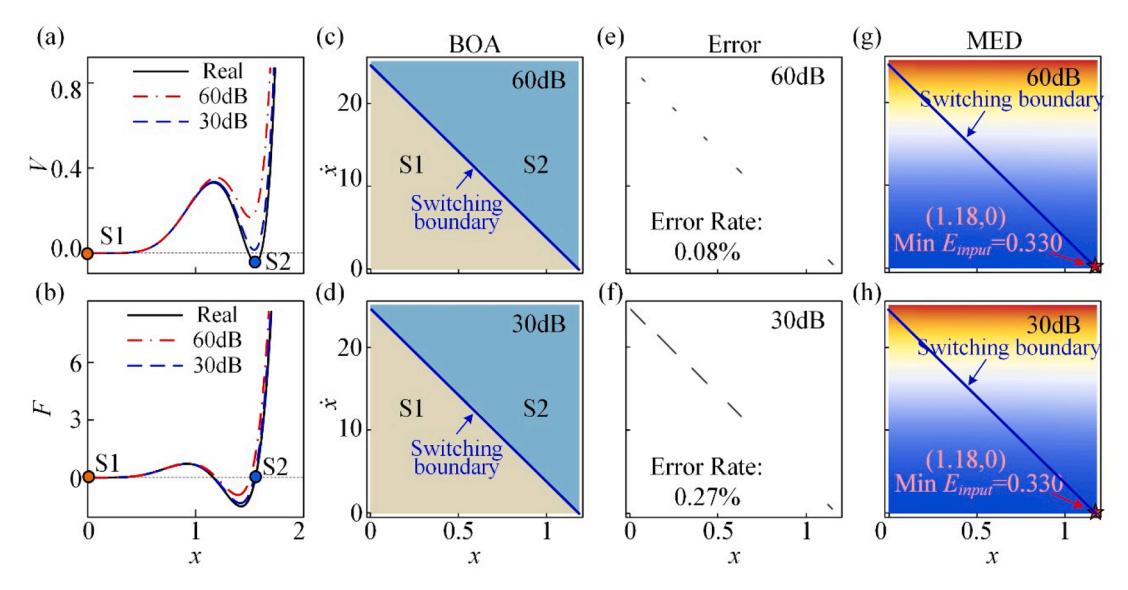


Fig. 5. Model reconstruction results for the bi-stable deployable unit cell under pink noise. (a) Comparison of potential energies among the real model, reconstructed models with different noise levels. (b) Comparison of restoring forces among the real model, reconstructed ones with different noise levels. (c-f) BOA prediction and corresponding error comparison under different noise levels. (g) and (h) show the MED predictions from the reconstructed models for two noise levels.

$$\begin{cases} \ddot{x}_{1} + \zeta_{1}(\dot{x}_{1} - \dot{x}_{b}) - \zeta_{2}(\dot{x}_{2} - \dot{x}_{1}) + \sum_{i=1}^{7} a_{i}(x_{1} - x_{b})^{i} - \sum_{i=1}^{7} b_{i}(x_{2} - x_{1})^{i} = \ddot{x}_{b}, \\ \ddot{x}_{2} + \zeta_{2}(\dot{x}_{2} - \dot{x}_{1}) + \sum_{i=1}^{7} b_{i}(x_{2} - x_{1})^{i} = 0, \end{cases}$$

$$(18)$$

where the corresponding coefficients are tabulated in Table 2.

Fig. 7 (a-b) compares actual and reconstructed equivalent restoring forces for the two cells, successfully capturing Cell 1's monostability and Cell 2's bistability properties. The results validate the capability of the proposed method to diagnose parametric design flaws in deployable structures. Assuming that Cell 2 is initially in undeployed state, a perturbation is applied at the base of the deployable structure, and the initial conditions of the system change to $x_1(0) = x_1^{s_0} + \Delta x, x_2(0) = x_2^{s_1} + \Delta x, \dot{x}_1(0) = \dot{x}_0, \dot{x}_2(0) = \dot{x}_0$. The BOAs and the corresponding error are

shown in Fig. 7(c-f), which exhibits a high accuracy. The obtained BOAs in Fig. 7(c) and (d) well reflect the deployment conditions of the M-DOF bi-stable deployable structure, which are then used to predict the MED condition. The input energy for deployment is also defined as the sum of the kinetic energy and the incremental potential energy of the bi-stable unit cells, which is consistent with that in Eq. (17). Phase-plane analysis (Fig. 7(g-h)) demonstrates consistent MED predictions between both noise conditions, further confirming the method robustness. Notably, the results reaffirm the energy-optimal deployment mechanism observed in SDOF systems: more initial displacement inputs minimize energy dissipation through reduced damping dissipation.

4. Experiments

This section experimentally investigates the proposed T-F-S SINDy method for dynamic model reconstruction of multi-stable structure to

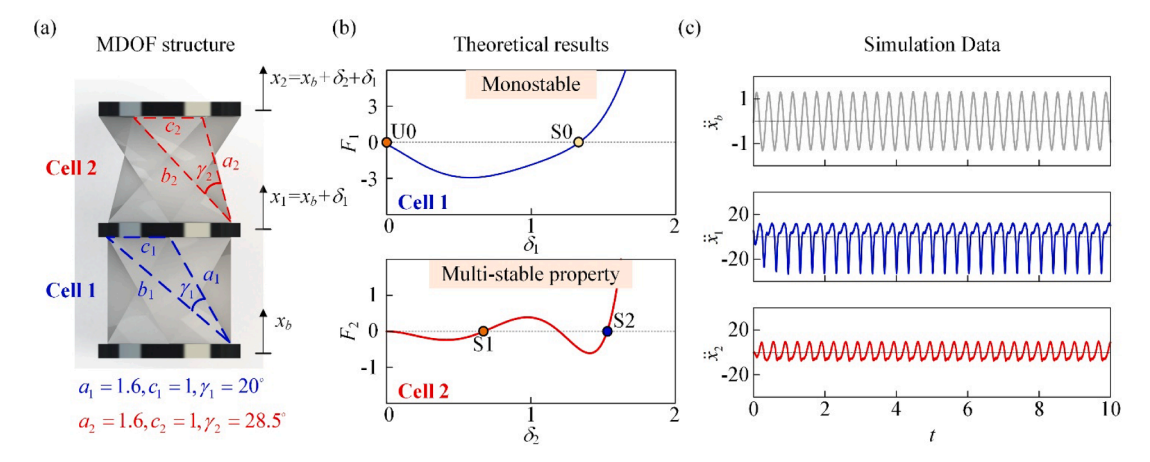


Fig. 6. (a) Schematic diagram of the M-DOF multi-stable deployable structure. (b) Equivalent restoring forces of two cells of the bi-stable deployable structure with different parameters; (c) Simulation data of responses and excitation of the M-DOF multi-stable deployable structure.

Table 2Coefficients of functions in the reconstruction model as Eq. (18) of the M-DOF deployable structure with multi-stable property case.

SNR		i	i					
		1	2	3	4	5	6	7
60dB	a_i b_i	-4.53 0	-9.58 -4.58	30.83 8.08	-25.13 0	6.95 0	0 -6.28	0 3.17
	ζ_i	0.99	1.00	\	\	\	\	\
30dB	a_i	-4.68	-9.14	30.36	-24.90	6.90	0	0
	b_i	0	-4.36	7.61	0	0	-5.84	2.94
	ζ_i	0.98	1.01	\	\	\	\	\

provide its minimum actuation energy for deployment. As shown in Fig. 8(a), by folding the 2-D crease pattern, a deployable structure based on Kresling Origami with undeployed and deployed state is constructed. The crease pattern cut by laser cutting machine breaks the basic assumption of Continuity and Compatibility at the crease, whose accurate dynamic model need to be reconstructed experimentally. For the Kresling structure as the illustration experimental prototype, we carry out both quasi-static tension testing and dynamic reconstruction testing.

For the quasi-static tension testing by Universal testing machine in Fig. 8 (b), the static force-displacement relation is shown as Fig. 8(c). The process and results for quasi-static tests are also shown in Video S1 (quasi-static test) in the Supplementary material. For the dynamic testing, the experimental process is illustrated in Fig. 8(d). The deployable structure is connected to an exciter, through which dynamic inputs are given to the deployable structure. The signal generator and controller provides input signal to the exciter. The system responses and excitation inputs are measured by Laser vibrometers. In the dynamic experimental testing, six sets of narrow-band sweep excitation inputs from 2 Hz to 12 Hz with different amplitudes and sweep speeds are applied to generate training data. Besides, a set of sweep excitations from 4 Hz to 8 Hz and 8 sets of sinusoidal excitations are used to generate testing data. The noise arises from two primary sources: the inherent noise present in the data acquisition process itself, and the noise introduced by the numerical differentiation of the acquired displacement data. Besides, additional Gaussian white noise SNR=60 dB is added into the data to verify the robustness of the proposed model reconstruction method. The whole dynamic tests are detailly illustrated in Video S1 (Dynamic test) in the Supplementary material. Then, based on the inputs and output signals, the T-F-S SINDy model reconstruction

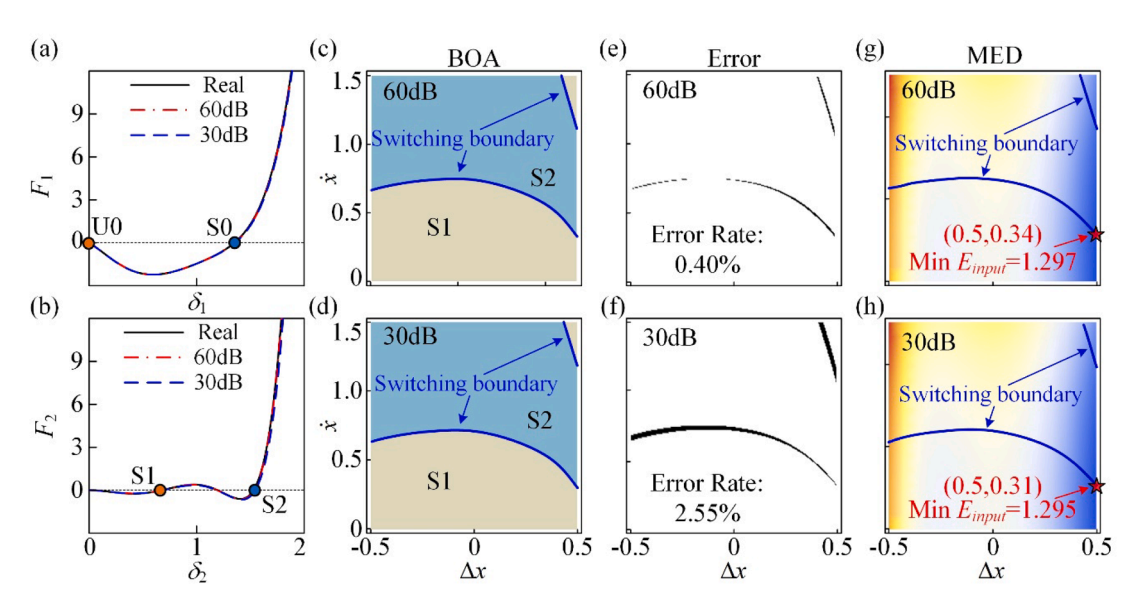


Fig. 7. Model reconstruction results for the M-DOF multi-stable deployable structure. (a) and (b) are the comparisons of the dynamic force-displacement relationships of the first and second layer for different noise levels. (c-f) BOA prediction and corresponding error comparisons for different noise levels. (g) and (h) show the MED prediction from the reconstruction model as Eq. (18).

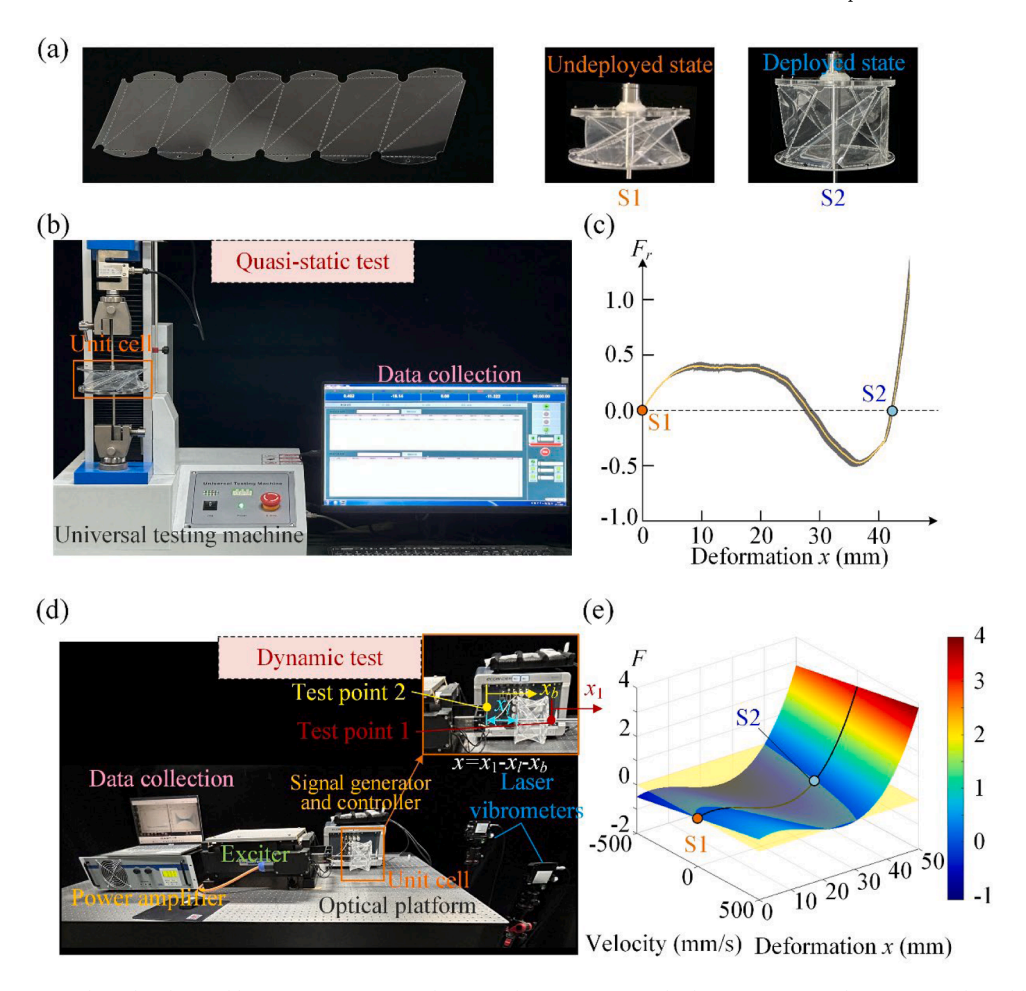


Fig. 8. Experimental setups and results obtained by quasi-static tests and proposed T-F-S SINDy method. (a) Experimental prototype of bi-stable deployable unit cell with undeployed and deployed states. (b) Experimental setup for quasi-static tests by universal testing machine. (c) Experimental reconstruction of static force-displacement relationship in quasi-static tests. (d) Experimental setup for dynamic tests. (e) Experimental reconstruction of dynamic equivalent constitutive relationship from the proposed T-F-S SINDy method inputs and outputs.

method is applied to obtain the equivalent dynamic constitutive model as Fig. 8(e). By the proposed method, the reconstruction model of the experimental deployable structure with multi-stable property writes

$$\ddot{x} + \zeta \dot{x} + \alpha x + \beta x^2 + \gamma x^3 = -\ddot{x}_b, \tag{19}$$

where the coefficients in the reconstructed dynamic model Eq. (19) are listed in Table 3

From Fig. 8(c) and (e), from both quasi-static testing and dynamic reconstruction, the structure exhibits two distinct stable configurations, defined as undeployed (S1) and deployed (S2). Comparative analysis reveals that both quasi-static testing and dynamic reconstruction successfully capture the bistable features and accurately predict stable equilibrium positions. However, discrepancies in stiffness between these two results lead to variations in unstable equilibrium prediction, highlighting the influence of difference in static and dynamic stiffness on the constitutive relationship. The difference between static stiffness and dynamic stiffness originates from the viscoelasticity of the materials in deployable structures. The experimental deployable structure is made of Polyethylene terephthalate (PET), which is a polymer with viscoelastic

Table 3Reconstruction model coefficients in experimental deployable structure with multi-stable property.

SNR	ζ	α	β	γ
60dB	1	44.46	-5.82	0.12

properties [42,43]. The stress-strain relationship of this viscoelastic material depends on the strain rate [44,45], and further combined with the geometric nonlinearity of the Kresling origami structure, leads to the difference in static and dynamic stiffness of the deployable structure. This finding emphasizes the necessity of employing dynamic reconstruction methods for multi-stable deployable structures operating under dynamic conditions.

After the dynamic model reconstruction process by the T-F-S SINDy method, for accuracy validation, two sets of verification tests are conducted. First, another set of sweep excitation from 4 Hz to 8 Hz is applied to the deployable structure to verify the capability of the proposed T-F-S SINDy method to predict frequency-domain response. The time history curve and spectrum of excitation are shown in Fig. 9(a)-(b), and the comparison results of the frequency-domain responses between experimental data and reconstructed model output signals are given in Fig. 9 (c). The data from reconstruction model demonstrates excellent agreement with the experimental frequency-domain response results, as error margin of approximately 5 % in predicting the resonant frequencies of the deployable structure. Notably, the reconstructed model effectively captures the double-frequency component in the deployable structure's frequency response, demonstrating the effectiveness of the proposed T-F-S SINDy method.

Second, eight sets of experimental deployment tests are conducted with harmonic base excitations of varying amplitudes and frequencies. The unit cell is initialized in S1, with successful deployment to S2 occurring when system states entered the S2 region in phase space, as

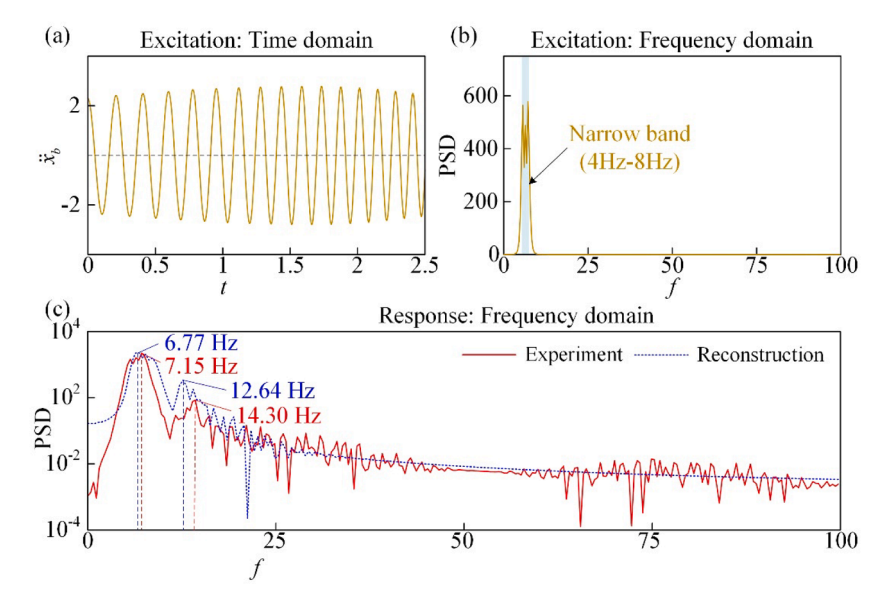


Fig. 9. Frequency-domain response prediction of the proposed T-F-S SINDy method. (a) Time history curve of the sweep excitation. (b) Spectrum of the sweep excitation. (c) Comparison between experimental and reconstructed frequency-domain response.

shown in Fig. 10. Test parameters are strategically selected to produce contrasting response characteristics: higher frequency excitations (Fig. 10 (a-b)) generate greater maximum velocities with limited displacements, while lower frequencies (Fig. 10 (c-d)) resulting in larger displacements at reduced velocities. The reconstruction model accurately predicts deployment process in all eight test cases, demonstrating its effectiveness in capturing the essential dynamics of configuration switching. According to the results of quasi-static tests and dynamic tests (based on the proposed T-F-S SINDy method), the deployment process and MED conditions are compared in Video S1 (Minimum Energy Deployment: Quasi-static vs Dynamic) in the Supplementary material,

where dynamic deployment shows an 80.39~% reduction in actuation energy compared with quasi-static deployment.

5. Conclusions and discussions

This study presents a novel Time-Frequency-domain Synergistic SINDy (T-F-S SINDy) method for dynamic model reconstruction of nonlinear dynamic systems with/without multi-stable property, specifically addressing the challenge of broadband noise interference in aerospace applications such as deployable structures. The proposed methodology synergistically integrates time-domain and frequency-

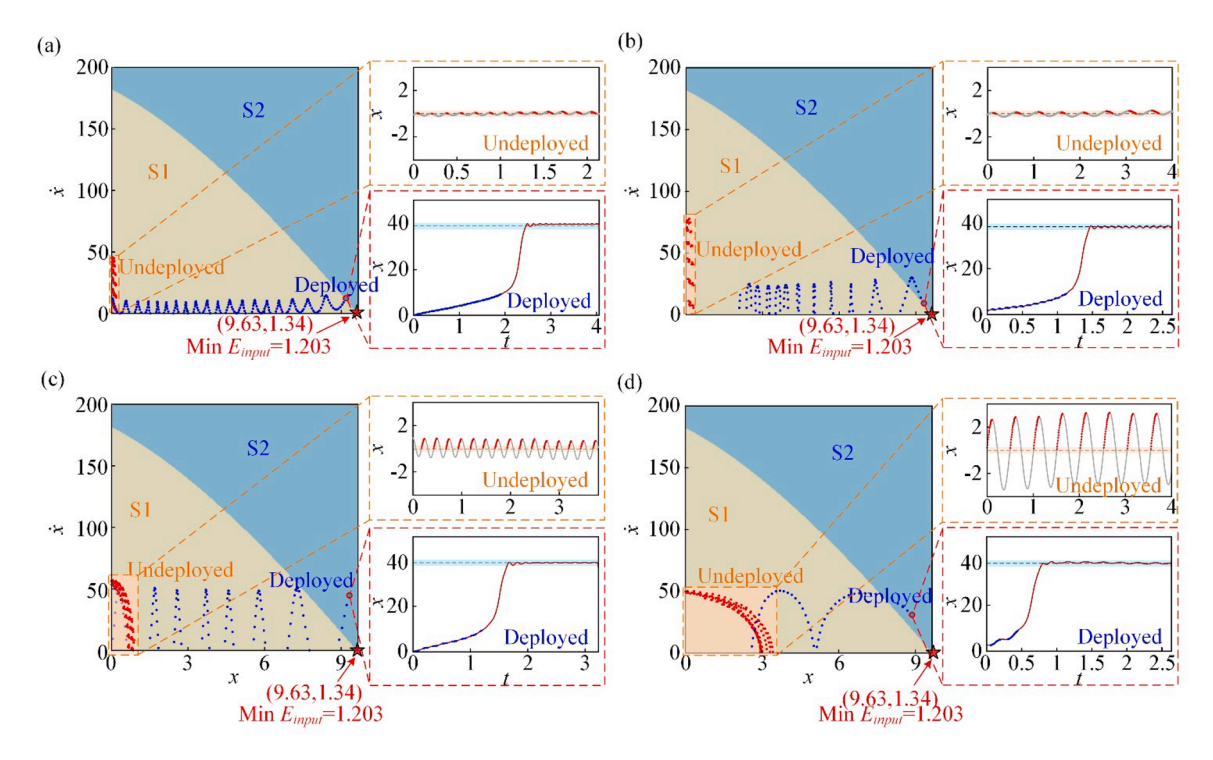


Fig. 10. Deployment condition prediction and experimental verification of deployment process. (a) and (b) show the higher frequency excitations with greater maximum velocities response with limited displacements response. (c) and(d) show the lower frequency excitations with larger displacements response at reduced velocities.

domain information to enhance reconstruction robustness through four innovative criteria: 1) a noise level estimation criterion exploiting the noise-induced degradation of collinearity between derivative terms and candidate functions; 2) a library selection criterion leveraging timedomain dynamics for candidate function elimination; 3) a feature extraction criterion employing frequency-domain analysis for noisesignal separation, and 4) an accuracy criterion statistically testing the fidelity of the reconstruction model. Numerical validations demonstrate the efficacy of the proposed method in reconstructing equivalent constitutive relationship of multi-stable deployable structures under different noise conditions, achieving BOA prediction errors below 3 %. Experimental validations through bi-stable unit cell testing reveal critical insights: while both quasi-static and dynamic methods can successfully identify stable equilibria, the differences of quasi-static and dynamic stiffness result in difference of constitutive relationship between the two stable equilibria. This fundamental distinction underscores the necessity of dynamic reconstruction for operational scenarios involving configuration switching. The effectiveness of the proposed T-F-S SINDy method in predicting deployment conditions is conclusively demonstrated through eight experimental cases with varying excitation parameters. Successful deployment predictions under contrasting dynamic regimes (high-frequency velocity-dominant vs. low-frequency displacement-dominant responses) confirm the accuracy and the capacity of proposed method. Owing to its robust ability in identifying equivalent dynamic model for broadband noises, the proposed T-F-S SINDy method shows great promise for structural design and actuation optimization for deployable structures, flexible robotics and vibration isolators. Despite the excellent robustness of the proposed T-F-S SINDy method, Fourier transform may fail to distinguish system response from non-stationary noise when non-stationary noise is present in the signal, compromising the effectiveness of the proposed T-F-S

SINDy method. In future work, the integration of time-frequency domain signal processing techniques such as short-time Fourier transform and wavelet transform could be explored to address non-stationary noise scenarios.

CRediT authorship contribution statement

Jiawei Qian: Writing – original draft, Visualization, Software, Methodology, Investigation, Formal analysis, Data curation, Conceptualization. Xiuting Sun: Writing – review & editing, Visualization, Supervision, Project administration, Investigation, Funding acquisition, Conceptualization. Li Cheng: Writing – review & editing, Validation, Supervision, Project administration, Funding acquisition. Qian Lv: Visualization, Software, Investigation. Jian Xu: Supervision, Resources, Project administration, Funding acquisition, Conceptualization.

Declaration of competing interest

The authors declare that they have no known competing financial interests or personal relationships that could have appeared to influence the work reported in this paper.

Acknowledgements

The authors would like to gratefully acknowledge the support from the National Natural Science Foundation of China under Grants (No. U2441202, 12372043, 12372022) and Fundamental Research Funds for Central Universities. The work also benefited from the support of the RIAIoT (Research Institute for Artificial Intelligence of Things) through project P0049625.

Supplementary materials

Supplementary material associated with this article can be found, in the online version, at doi:10.1016/j.ast.2025.111268.

Appendix A

This Appendix illustrates the derivation of the dynamic model of Kresling origami based on truss model The crease pattern of Kresling origami structure and the 3-D mechanical model are shown in Fig. A1. The crease pattern is determined by three parameters a_0 , c_0 and γ_0 , where b_0 can be expressed

$$b_0 = \frac{c_0}{\sin\gamma_0} \sin\left(\gamma_0 + \arcsin\left(\frac{a_0 \sin\gamma_0}{c_0}\right)\right). \tag{A.1}$$

In the truss model, the creases of the Kresling origami structure are simplified as springs with stiffnesses k_a and k_b and rest lengths a_0 and b_0 . When the height h and angle θ of the Kresling origami structure are determined, the crease length can be expressed as

$$a = \sqrt{h^2 + 4R^2 \sin^2\left(\frac{\theta}{2}\right)},\tag{A.2}$$

$$b = \sqrt{h^2 + 4R^2 \sin^2\left(\frac{\theta}{2} + \frac{\pi}{6}\right)},\tag{A.3}$$

where R is the circumradius of the base regular hexagon. Based on the truss model, the potential energy U of the Kresling origami structure can be expressed as

$$U = 6\left(\frac{1}{2}k_a(a-a_0)^2 + \frac{1}{2}k_b(b-b_0)^2\right). \tag{A.4}$$

Neglecting the moment of inertia of the end plate, the kinetic energy E_{ν} and the generalized force Q are

$$E_{\nu} = \frac{1}{2}m\dot{h}^2,\tag{A.5}$$

$$Q = -c_d \dot{h}. \tag{A.6}$$

Substituting Eqs. (A.4-A.6) and $h = x-x_0$ into Lagrange equation, the dynamic equation could be obtained

$$m\ddot{x} + c_q(\dot{x} - x_0) + 3k_a(a - a_0)\frac{\partial a}{\partial \theta} + 3k_b(b - b_0)\frac{\partial b}{\partial \theta} = 0. \tag{A.7}$$

Since no external torque is applied to the Kresling origami structure, the free torque condition T = 0 needs to be satisfied:

$$T = \frac{\partial U}{\partial \theta} = 6R^2 k_a \left(1 - \frac{a_0}{a} \right) \sin\theta + 6R^2 k_b \left(1 - \frac{b_0}{b} \right) \sin\left(\theta + \frac{\pi}{3}\right) = 0. \tag{A.8}$$

Therefore, the dynamic model of the Kresling origami structure can be expressed by Eq. (A.7) and Eq. (A.8).

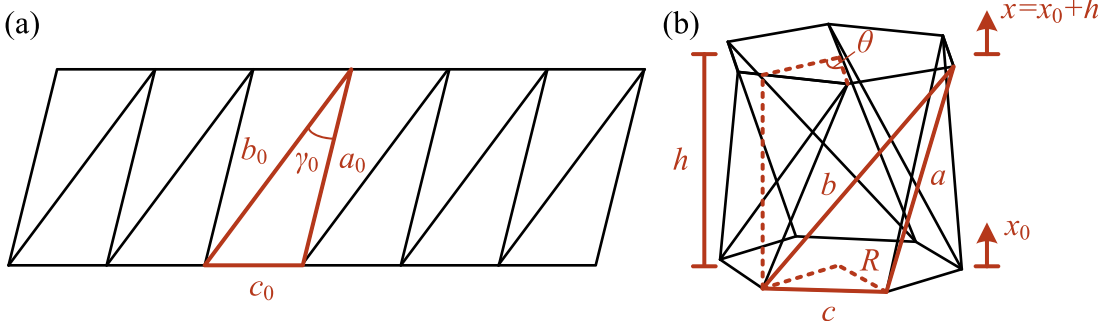


Fig. A1. (a) 2-D crease pattern and corresponding geometric parameters. (b) 3-D truss mechanical model for Kresling origami structure.

Appendix B

To compare the computational cost and reconstruction model accuracy between the proposed T-F-S SINDy method and the classical SINDy method, the multi-stable deployable structure in Section 3.1 is adopted. Under SNR = 30 dB, both methods are employed for model reconstruction using identical training data. The reconstruction result of T-F-S SINDy has already been demonstrated in Eq. (16) and Table 1. The reconstruction result of classical SINDy is

$$\ddot{x} + 17.09\dot{x} - 27.73x + 223.46x^3 - 179.24x^4 - 151.83x^5 + 182.60x^6 - 43.21x^7 = 0$$
(B.1)

In order to compare the computation cost, the dimension of the function library matrix and computation time are concerned. Besides, a Regularized MSE (R-MSE) is defined to evaluate the accuracy of the reconstruction model on test data, which is defined as

$$R - MSE = \frac{\frac{1}{n} \sum_{i=1}^{n} (x_{test} - x_{predict})^{2}}{\frac{1}{n} \sum_{i=1}^{n} x_{test}^{2}}.$$
(B.2)

The R-MSE is the MSE normalized by variance of response data. Then, the dimension of the function library matrix, computation time, and regularized MSE are summarized in Table 2.

 Table B1

 Comparison of computational cost and reconstruction accuracy between T-F-S SINDy and classical SINDy.

Method	Dimension of function library matrix	computation time	R-MSE
T-F-S SINDy	2143×28	4.4 s	0.0045
Classical SINDy	200,020×36	120.72 s	0.0332

As illustrated in Table B1, the T-F-S SINDy method outperforms SINDy in both computational efficiency and reconstruction accuracy. Regarding computational efficiency, T-F-S SINDy substantially reduces the dimension of the function library matrix through additional criteria, thereby decreasing regression computational costs. Furthermore, during sparsification parameter optimization, it is required to solve regression problems under varying sparsification parameters. A smaller function library matrix can significantly enhance computational efficiency.

Data availability

Data will be made available on request.

References

- [1] G.E. Fenci, N.G. Currie, Deployable structures classification: a review, Int. J. Space Struct. 32 (2) (2017) 112–130.
- [2] T. Chubachi, H. Furuya, H. Sakamoto, Boom-membrane space structure's incomplete deployment after storage in OrigamiSat-1 ground demonstrator, AIAA J. 62 (7) (2024) 2401–2413.
- [3] Z. Liu, Q. Li, X. Lan, et al., Structural and dynamic analysis of a flexible solar array based on shape memory polymer composites, Compos. Struct. 280 (2022) 114918.
- [4] G. Lu, J. Zhou, G. Cai, et al., Active vibration control of a large space antenna structure using cable actuator, AIAA J. 59 (4) (2021) 1457–1468.
- [5] P. Wang, J. Li, Q. Wang, et al., Kirigami-inspired bidirectional extensible planar deployable structures with driving mechanisms, Mech. Mach. Theory 209 (2025) 105969.
- [6] S. Tsuda, J. Kohno, Y. Nakahara, et al., Composition of curvilinearly extendable tubular scissor mechanisms, Int. J. Solids. Struct. 250 (2022) 111673.
- [7] D. Melancon, B. Gorissen, C.J. Garcia-Mora, et al., Multistable inflatable origami structures at the metre scale, Nature 592 (7855) (2021) 545–550.
- [8] W.X. Xu, J. Zhang, H.W. Guo, et al., Design of a deployable aerodynamic decelerator based on a tensegrity structure, Acta Astronaut. 215 (2024) 315–324.

- [9] H. Zhao, C. Shi, H. Guo, et al., Dynamic performance prediction of an annular tensegrity structure based on similitude method, Eng. Struct. 288 (2023) 116232.
- [10] L. Dai, R. Xiao, Optimal design and analysis of deployable antenna truss structure based on dynamic characteristics restraints, Aerosp. Sci. Technol. 106 (2020) 106086.
- [11] T.H. Kim, J.E. Suh, J.H. Han, Deployable truss structure with flat-form storability using scissor-like elements, Mech. Mach. Theory 159 (2021) 104252.
- [12] J. Shore, A. Viquerat, G. Richardson, et al., The natural frequency of drumdeployed thin-walled open tubular booms, Thin-Walled Struct. 170 (2022) 108650.
- [13] T.W. Liu, J.B. Bai, N. Fantuzzi, Analytical models for predicting folding behaviour of thin-walled tubular deployable composite boom for space applications, Acta Astronaut. 208 (2023) 167–178.
- [14] Q. Duan, C. Tang, J. Sun, et al., Design and dynamics of a deployable assembly module via rollable booms, Acta Astronaut. 225 (2024) 634–655.
- [15] L.H. Blumenschein, L.T. Gan, J.A. Fan, et al., A tip-extending soft robot enables reconfigurable and deployable antennas, IEEE Robot. Autom. Lett. 3 (2) (2018) 949–956
- [16] W. Liu, D. Kong, W. Zhao, et al., Multi-stimulus responsive shape memory polyurea incorporating stress-mismatching structure for soft actuators and reversible deployable structures, Compos. Struct. 334 (2024) 117966.
- [17] Z. Qi, X. Sun, J. Xu, A Kirigami multi-stable flexible gripper with energy-free configurations switching, Adv. Intell. Syst. 6 (8) (2024) 2400038.
- [18] B. Shahryari, H. Mofatteh, A. Sargazi, et al., Programmable shape-preserving soft Robotics arm via multimodal multistability, Adv. Funct. Mater. 35 (6) (2024) 2407651
- [19] C. Zhang, Z. Zhang, Y. Peng, et al., Plug & play origami modules with all-purpose deformation modes, Nat. Commun. 14 (1) (2023) 4329.
- [20] L. Zhang, Q. Gao, H.W. Zhang, An efficient algorithm for mechanical analysis of bimodular truss and tensegrity structures, Int. J. Mech. Sci. 70 (2013) 57–68.
- [21] G. Xin, H. Deng, G. Zhong, Closed-form dynamics of a 3-DOF spatial parallel manipulator by combining the lagrangian formulation with the virtual work principle, Nonlinear. Dyn. 86 (2) (2016) 1329–1347.
- [22] Y. Jin, L. Hou, S. Zhong, et al., Invertible Koopman Network and its application in data-driven modeling for dynamic systems, Mech. Syst. Signal. Process. 200 (2023) 110604.
- [23] C. Chen, Y. Wang, B. Fang, et al., Low-dimensional dynamical models of structures with uncertain boundaries via a hybrid knowledge- and data-driven approach, Mech. Syst. Signal. Process. 223 (2025) 111876.
- [24] D. Jiang, M. Zhang, Y. Xu, et al., Rotor dynamic response prediction using physicsinformed multi-LSTM networks, Aerosp. Sci. Technol. 155 (2024) 109648.
- [25] S. Zhao, C. Cheng, M. Lin, et al., Physics-informed deep sparse regression network for nonlinear dynamical system identification. J. Sound. Vib. 595 (2025) 118796.
- [26] X. Gao, C. Peng, W. Xu, et al., Dynamic time history response prediction through an experimentally trained deep gated recurrent units network using cyber physical real-time hybrid simulation, Mech. Syst. Signal. Process. 224 (2025) 112247.
- [27] M. Lin, C. Cheng, Z. Peng, Nonlinear dynamical system identification using the sparse regression and separable least squares methods, J. Sound. Vib. 505 (2021) 116141

- [28] X. He, Z. Sun, Sparse identification of dynamical systems by reweighted 11regularized least absolute deviation regression, Commun. Nonlinear Sci. Numer. Simul. 131 (2024) 107813.
- [29] S. Liu, J. Xiao, Z. Yan, et al., Noise resistance of next-generation reservoir computing: a comparative study with high-order correlation computation, Nonlinear. Dyn. 111 (15) (2023) 14295–14308.
- [30] J. Friedman, T. Hastie, R. Tibshirani, Regularization paths for generalized linear models via coordinate descent, J. Stat. Softw. 33 (1) (2010) 1–22.
- [31] S.L. Brunton, J.L. Proctor, J.N. Kutz, Discovering governing equations from data by sparse identification of nonlinear dynamical systems, Proc. Natl. Acad. Sci. U.S.A 113 (15) (2016) 3932–3937.
- [32] S.H. Rudy, S.L. Brunton, J.L. Proctor, et al., Data-driven discovery of partial differential equations, Sci. Adv. 3 (4) (2017) e1602614.
- [33] Z. Huang, Y. Tian, C. Li, et al., Data-driven automated discovery of variational laws hidden in physical systems, J. Mech. Phys. Solids 137 (2020) 103871.
- [34] A. Pecile, N. Demo, M. Tezzele, et al., Data-driven discovery of delay differential equations with discrete delays, J. Comput. Appl. Math. 461 (2025) 116439.
- [35] L. Boninsegna, F. Nuske, C. Clementi, Sparse learning of stochastic dynamical equations, J. Chem. Phys. 148 (24) (2018) 241723.
- [36] H.H. Ren, Y.L. Bai, M.H. Fan, et al., Constructing polynomial libraries for reservoir computing in nonlinear dynamical system forecasting, Phys. Rev. E 109 (2) (2024) 024227.
- [37] A.A. Kaptanoglu, J.L. Callaham, A. Aravkin, et al., Promoting global stability in data-driven models of quadratic nonlinear dynamics, Phys. Rev. Fluids 6 (9) (2021) 094401
- [38] J. Qian, X. Sun, J. Xu, et al., Discovering differential governing equations of hysteresis dynamic systems by data-driven sparse regression method, Nonlinear. Dyn. 112 (14) (2024) 12137–12157.
- [39] J. Qian, X. Sun, J. Xu, A data-driven reconstruction method for dynamic systems with multistable property, Nonlinear. Dyn. 111 (5) (2023) 4517–4541.
- [40] H. Han, V. Sorokin, L. Tang, et al., Origami-based tunable mechanical memory metamaterial for vibration attenuation, Mech. Syst. Signal. Process. 188 (2023) 110033.
- [41] H. Han, V. Sorokin, L. Tang, et al., Lightweight origami isolators with deployable mechanism and quasi-zero-stiffness property, Aerosp. Sci. Technol. 121 (2022) 107319.
- [42] J. Qing, S. Zhou, J. Wu, et al., Primary and secondary resonance responses of fractional viscoelastic PET membranes, Commun. Nonlinear Sci. Numer. Simul. 116 (2023) 106810.
- [43] R. Dang, Y. Cui, J. Qu, et al., Variable fractional modeling and vibration analysis of variable-thickness viscoelastic circular plate, Appl. Math. Model. 110 (2022) 767–778.
- [44] Y. Sengül, Nonlinear viscoelasticity of strain rate type: an overview, in: Proceedings of the Royal Society A: Mathematical, Physical and Engineering Sciences 477, 2021 20200715.
- [45] J.P. Noyel, A. Hajjar, R. Debastiani, et al., Impact of viscoelasticity on the stiffness of polymer nanocomposites: insights from experimental and micromechanical model approaches, Polym. (Guildf) 309 (2024) 127443.